Phase-transition-induced Thermal Hysteresis in Type-II Weyl Semimetals $MoTe_2$ and $Mo_{1-x}W_xTe_2$

Md Sabbir Akhanda[a], Sergiy Krylyuk[b], Diane A. Dickie[c],

Albert V. Davydov[b], Fei Han[d], Mingda Li[d], Mona Zebarjadi[a,e,*]

[a] *Department of Electrical and Computer Engineering, University of Virginia, Charlottesville, Virginia 22904, USA*

[b] *Materials Science and Engineering Division, National Institute of Standards and Technology, Gaithersburg, MD 20899, USA*

[c] *Department of Chemistry, University of Virginia, PO Box 400319, Charlottesville, Virginia 22904-4319, USA*

[d] *Department of Nuclear Science and Engineering, Massachusetts Institute of Technology, Cambridge, Massachusetts 02139, USA*

[e] *Department of Materials Science and Engineering, University of Virginia, Charlottesville, Virginia 22904, USA*

* Corresponding author e-mail address: m.zebarjadi@virginia.edu

Keywords: Weyl semimetal, Phase transition, Seebeck effect, Thomson effect, Nernst effect

Abstract

The resistivity versus temperature measurement is commonly used for identifying temperature-induced phase change and the resulting hysteresis loop. While the resistance is influenced by both the density of states and the carrier lifetimes, the Seebeck coefficient is influenced predominantly by the density of states, and hence is a better probe of the phase of the material. Here, 1T′ - T_d temperature-induced phase transition in $MoTe_2$ is studied using temperature-dependent X-ray diffraction, resistivity, and Seebeck coefficient measurements. A more distinct hysteresis is observed when measuring the Seebeck coefficient which is consistent with direct measurements of the crystallographic angle using the temperature-dependent X-ray diffraction. The Seebeck

and electrical resistivity measurements indicate a competing contribution of the electrons and holes. The contribution of electron pockets becomes more dominant when molybdenum atoms are replaced by tungsten. In $MoTe_2$, a topologically induced enhancement of the Nernst coefficient is observed at low temperatures, and a relatively large phase-transition induced Thomson coefficient of 111 $\mu V \cdot K^{-1}$ is measured at 254 K which is larger than the Seebeck coefficient measured in the entire temperature range.

1. Introduction

Transition metal dichalcogenides (TMDCs) are a large family of layered materials with the chemical formula MX_2 where M is a transition metal (e.g., Mo, W, Nb, Ta, Ti, Zr, Hf, etc.) and X is a chalcogen atom (e.g., S, Se, Te). [1] Each unit layer is composed of three sheets of atoms arranged in the $X-M-X$ configuration with the metal atoms in the middle and the chalcogen atoms on the two sides. The layers are held together by a weak van der Waals interaction. [2] Depending on coordination in $X-M-X$ layers and stacking orders along the c-axis, TMDCs can exist in different phases like 1T, 2H, 3R, and T_d. Over 40 different TMDCs have been discovered so far. [3] These materials together with their different polymorphs have been found to show diverse electronic and photonic properties. In recent years, some of the TMDCs that are lacking either space or time inversion symmetry have been experimentally proven to host the Weyl semimetallic state, a non-trivial symmetry-protected topological phase of matter characterized by a pair of degenerate Weyl cones of opposite chirality with linear dispersion around the Weyl nodes in the bulk and Fermi arcs on the surface. [4–6] These TMDCs are particularly interesting because of the many topologically induced exotic properties such as extremely large magnetoresistance, [7–13] superconductivity, [14–20] and planar and spin-Hall effect [21–23] observed in the Weyl semimetals so far. The crystalline to crystalline polymorphic structural transitions reported in some of these materials has helped garner even more interest from emerging fields like neuromorphic computing, [24], and

phononic and thermal logic devices. [25] In particular, $MoTe_2$, [26–29] and $Mo_{1-x}W_xTe_2$ alloys [30,31] are known to be type II Weyl semimetals (i.e., the Weyl cones are tilted in the momentum space leading to the breaking of the Lorentz symmetry) [32,33] exhibiting a crystalline-to-crystalline phase transition and are the focus of this paper.

$MoTe_2$ has three polytypes: 2H (space group $P6_3/mmc$), 1T′ (space group $P2_1/m$) and T_d (space group $Pmn2_1$). [34–36] The semiconducting 2H phase is the thermodynamically preferred state at room temperature. The monoclinic 1T′ phase is naturally stable above 900 °C but can also be stabilized at room temperature by employing techniques such as rapid cooling, tellurization rate control, or appropriate precursor selection for the chemical vapor deposition. [37] Upon cooling, the $1T' - MoTe_2$ undergoes a first-order phase transition around 250 K to the orthorhombic T_d phase which is a type-II Weyl semimetal. [15,36,38,39] The degree of substitution of molybdenum by tungsten controls the phase in which the $Mo_{1-x}W_xTe_2$ alloys exist at room temperature (pure 1T′: $x \leq 0.1$, mixed $1T' + T_d$: $0.1 < x < 0.6$ and pure T_d: $x \geq 0.6$). [40]

Here, we study pure $MoTe_2$ and $Mo_{1-x}W_xTe_2$ alloys with $0 \leq x \leq 0.08$ and at first demonstrate the potential of the Seebeck coefficient as an efficient tool for probing the thermal hysteresis induced by a phase transition from the 1T′ phase to the T_d phase. Three separate measurements: X-ray diffraction (XRD), electrical resistivity, and Seebeck coefficient are presented to support this case. Then, we report a topologically induced enhancement of the Nernst coefficient in the temperature range of 2 K – 50 K and phase-transition induced enhancement of the Thomson coefficient. Finally, we report the effect of W substitution on the thermoelectric transport behavior of the $Mo_{1-x}W_xTe_2$ alloys.

2. Materials and methods

2.1. Sample preparation.

Large $Mo_{1-x}W_xTe_2$ crystals were grown by the iodine-assisted Chemical Vapor Transport (CVT) method at 1000 °C using polycrystalline the respective $Mo_{1-x}W_xTe_2$ powders. In order to retain the 1T′ phase of the crystals, the ampoules were ice-water quenched after 7 days to 14 days of growth. More details on the sample preparation and phase transition studies can be found in the article by Oliver et al. [40]

2.2. Materials characterizations

Chemical compositions of the grown crystals were determined by energy-dispersive X-ray spectroscopy (EDS) using a JEOL JSM-7100F field emission scanning electron microscope (FESEM) equipped with an Oxford Instruments X-Max 80 EDS detector.

2.3. Transport property measurements

Temperature-dependent Seebeck and Nernst coefficients were measured in the one-heater two thermometer configuration using Versalab and PPMS from Quantum Design Inc. Singles crystals samples were placed on a glass substrate using GE varnish. Gold-coated flat copper wires of 0.5 mm width were used for making the contacts. One end of the sample was connected to a resistive heater while the other end was attached to the cold foot of the puck that acts as the heatsink. Two Cernox sensors, capable of measuring both temperature and voltage, were placed in between the heater and heatsink to estimate the temperature gradient and Seebeck voltage of the samples. For the Nernst measurement, the voltage lead of the cold side sensor was separated and connected opposite to the hot side sensor along the width of the samples. A magnetic field was applied along the c-axis of the crystal. The resistivity of the samples was measured using a four-point probe configuration where a current was passed from the heater side towards the heatsink. The estimated errors in the Seebeck, resistivity, and Nernst measurements are about 5 %, 3 %, and 10 % respectively. The main error sources include fitting errors of MultiVu software, error in measurement of the sample size, non-uniformity of the temperature gradient, and instrumental errors.

3. Result and discussion

3.1. Seebeck coefficient as a phase transition probe

We employ three different measurements (XRD, electrical resistivity, and Seebeck coefficient) to investigate the thermal hysteresis induced by the $1T'-T_d$ structural phase transition in $MoTe_2$ (see Figure 1). The hysteresis observed in the monoclinic $\beta-$ angle during a temperature-dependent XRD measurements is a direct probe of structural phase transition. As shown in Figure 1a, during the cooling half-cycle, the β-angle remains constant up to 260 K and then gradually changes from 93.92° to 90° between 260 K and 210 K indicating the presence of both phases in this temperature range. It remains at 90°, a signature of orthorhombic T_d phase, up to 130 K. On the warming half-cycle, the sample goes through the reverse $T_d - 1T'$ transition with β-angle changing its value gradually from 90° to 93.92° within the temperature range of 257 K to 300 K. This range is different from what we observed in the cooling half-cycle. Thus, tracking the β-angle over the full thermal cycle, we obtain a hysteresis extending over the temperature range of 210 K to 300 K. [41] It is to be noted that, tracking the β-angle , Clarke et al. reported a hysteresis over a shorter temperature range (233 K to 280 K) compared to this work. [36] Using van der Waals density functional method, it has been shown that the T_d phase is energetically more stable than the 1T′ phase and the energy difference between these two phases in $MoTe_2$ is 0.4 meV per unit cell. Calculation of free energy of the two systems (to include the temperature effects) showed a lower energy of 1T′ phase at temperatures above 150 K. While the 150 K is lower than the experimentally measured phase transition temperature, the calculations confirm the structural phase transition. The origin of the phase transition is related to the interlayer bonding states near the Fermi energy and can be tuned by charge doping. [41]

Dahal et al. studied the $1T'-T_d$ phase transition in $MoTe_2$ using resistivity data. [42] They defined the phase-transition temperature (T_s) as the temperature where $\frac{d\rho(T)}{dT}$ maxima occurs and reported $T_s \approx 249$ K in the cooling half-cycle. [42] They observed a thermal hysteresis extending from 150 K to 300 K (their highest measured temperature). However, at 300 K their hysteresis loop did not converge meaning that the hysteresis probably would have ended at a higher temperature. The thermal hysteresis loop we observed in the temperature-dependent resistivity measurement (Figure 1b) is slightly different from the one reported by Dahal et al. and extends from ~ 230 K to ~ 330 K. The magnitude of the change in resistivity across the thermal hysteresis is small as evident from the graph because both $1T'$ and T_d phases are semimetallic. When the change in electrical resistivity is small, e.g., a semimetal-semimetal phase transition in $MoTe_2$, the probability of the measurement errors playing a deteriorating effect increases, making it challenging to study the phase transition. Thus, resistivity measurement does not always best portray the underlying changes. On the contrary, as seen in Figure 1c, the effect of such phase change on the magnitude of the Seebeck coefficient obtained from a temperature-dependent measurement is noticeably pronounced and resulted in a clear hysteresis spanning from approximately 134 K to 345 K. This is a clear indication that the Seebeck coefficient is a better probe than resistivity for studying temperature-driven structural phase changes in materials. It is known that while the electrical conductivity is influenced both by the band structure and the carrier lifetimes, the Seebeck coefficient to the first-order approximation, depends only on the band structure and is not sensitive to the details of the lifetimes. Both the T_d and $1T' - MoTe_2$ phase contains multiple electron-hole pockets [7] and the balance in the electron-hole contribution is modified through the phase transition. This is not observable in resistivity measurement as both electrons and holes contribute a positive resistance. It shows well in the Seebeck measurement as the electrons and holes have different Seebeck signs and therefore the Seebeck measurement

can determine the relative change in the electron-hole concentration effectively. Thus, the Seebeck coefficient both theoretically and as shown experimentally in Figure 1c, is a better probe for studying the temperature-dependent phase change in $MoTe_2$. It is important to acknowledge here that, though the effect of the carrier lifetime is secondary, we cannot completely discard it playing a role in the Seebeck coefficient measurement.

Phase-transition induced enhanced variation in the Seebeck coefficient results in a large Thomson coefficient in $MoTe_2$. Similar enhancements have been recently reported in the case of FeRh. [43] Thomson heating/cooling is a nonlinear response and is proportional to the product of an applied electrical current and temperature gradient. The Thomson coefficient τ of a material at a given temperature T, is defined as the product of the sample temperature and the first derivative of the Seebeck coefficient with respect to T. [44] The Thomson effect enables cooling/heating in homogenous samples, allowing for simpler device design. This effect is usually small compared to the normal Seebeck effect and hence has not been studied widely. As seen in Figure 1d, the steep variation in the Seebeck coefficient due to phase change results in a τ of 111 μVK^{-1} at 254 K (warming half-cycle). The presence of hysteresis is reflected in peaks appearing at different temperatures of the cooling and warming half-cycles. Our observed magnitude is significantly greater than what was reported for Ni ($-16\ \mu VK^{-1}$) and $Bi_{88}Sb_{12}$ ($45\ \mu VK^{-1}$) and is comparable to the one observed in a p-type Bi_2Te_3 ($150\ \mu VK^{-1}$). [45,46] We note that the Seeback coefficient values of Ni, $Bi_{88}Sb_{12}$ and p-type Bi_2Te_3 are larger than their respective Thomson coefficients. This is not the case for $MoTe_2$ studied here that demonstrates Thomson coefficient values that are an order of magnitude larger than the Seebeck coefficient.

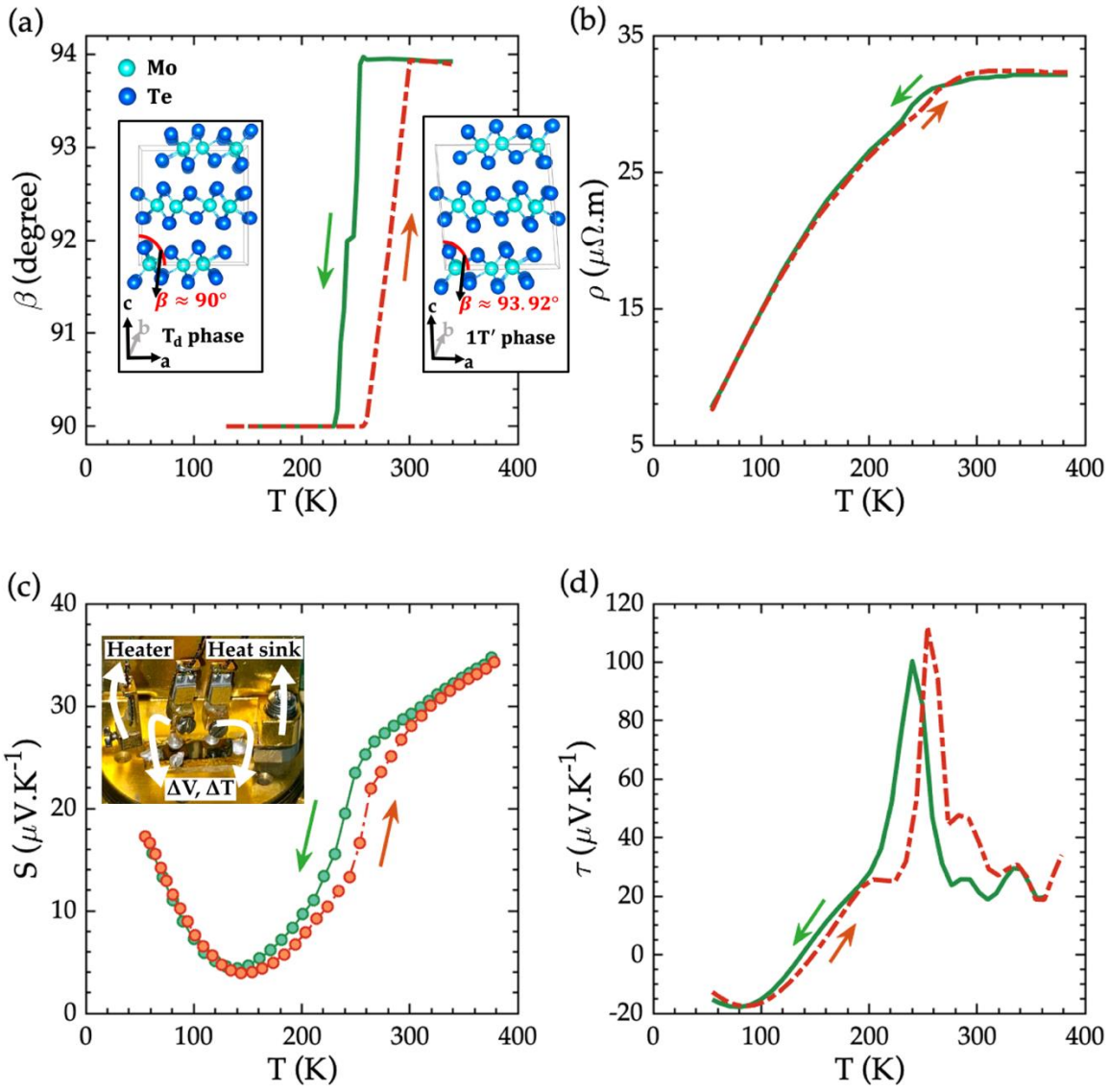

Figure 1 Temperature dependence of a) monoclinic angle β, b) resistivity, c) Seebeck coefficient, and d) Thomson coefficient of $MoTe_2$ over the cooling (solid line) and warming (dashed line) half-cycles. Inset in Figure 1a shows the crystal structure of T_d and 1T′ phases of $MoTe_2$ with their respective β angle indicated. Inset in Figure 1c shows a sample mounted on the sample holder (puck) for measurement.

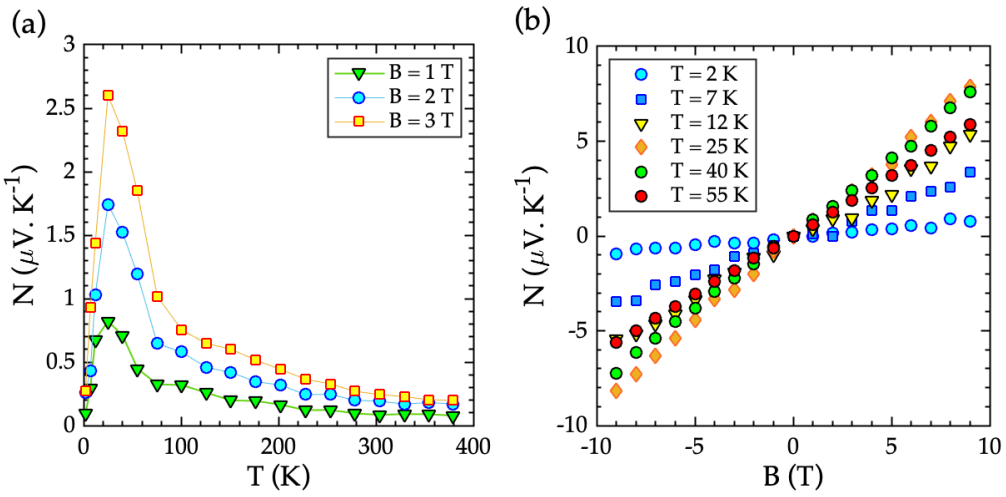

Figure 2 a) Temperature and b) magnetic field dependence of the Nernst Coefficient of $MoTe_2$

3.2. Nernst coefficient at low-temperature

The Nernst effect is important thermomagnetic effect for directly converting thermal energy to electrical energy and cooling. In this effect, a voltage is generated in response to the presence of a magnetic field applied perpendicular to a thermal gradient such that the direction of the voltage, thermal gradient, and magnetic field are all orthogonal to each other. [47] Since, the Lorentz force exerted by the magnetic field pushes mobile carriers with opposite charges to the opposite sides, the contribution of the electrons and holes are additive in setting the magnitude of the Nernst coefficient (*N*). Consequently, two-carrier systems like Dirac and Weyl semimetals are promising candidates for thermomagnetic applications. [48–51] Similar to the Thomson modules, the Nernst modules can use a single homogenous material. This is in contrast to the thermoelectric modules that are always using a p-n pair.

Here, we investigated the temperature dependence of the Nernst coefficient (*N*) of $MoTe_2$ from 380 K to 2 K. At room temperature (300 K), the magnitude of *N* is ≈ 0.084 $\mu VK^{-1}T^{-1}$. With decreasing temperature, the value of *N* increases and ultimately peaks at ≈ 25 K. At this temperature, the value of *N* is found to be 0.82 $\mu VK^{-1}T^{-1}$ which is about 10 times larger than that observed at 300 K. Further decrease in the temperature leads to

a rapid decrease in N. Since the Nernst coefficient increases at lower temperatures due to higher mobility, [52,53] this rapid decreasing trend is not generally expected [54] and serves as an indication that there are additional factors to be considered. To understand the origin of the peak, a closer look at the band structure of $MoTe_2$ is required. The semimetallic $MoTe_2$ has several electron and hole pockets that can be described by quadratic dispersion. [7,8] Being a Weyl semimetal, the band structure also exhibits linear dispersion around the Weyl nodes. The peak around 25 K marks the region where linear dispersion dominates over the quadratic ones. In the temperature range of 380 K to approximately 100 K, the N is dominated by quadratic bands while in the temperature range from 100 K to 2 K, the effect of linearly dispersive bands gradually appears. In this region, with decreasing temperature, the Fermi level shifts more towards the Dirac point causing the N to rise. When the Fermi level is close to the Dirac point at $\approx$ 25 K, the enhanced mobility of the charge carriers [7] leads to the largest value of N observed. Further decrease in temperature (25 K to 2 K) moves the Fermi level away from the Weyl point resulting in a subsequent decrease in N. Similar theoretical argument in the case of single-crystal NbP, a Weyl semimetal, has been able to well-replicate the experimental data. [48] Since the phase transition effects and the low-temperature topological effects appearing in $MoTe_2$ are separated by a sizable temperature gap, we do not anticipate one affecting the other. The addition of W shifts the phase transition to a higher temperature as reported in the literature [42], further ruling out any interplay between these two effects when W is added. With W addition, we did not observe any noticeable change in the temperature dependence of the Nernst coefficient (see Fig. S1 in the Supplemental Material).

The magnetic field dependence of the Nernst coefficient is plotted in Figure 2b. Using the Jones-Zener expansion, one can show that N enters into a non-linear response region when the product of carrier mobility (μ) and magnetic field (B) is much larger than unity. [55] The Nernst coefficient of $MoTe_2$, as can be seen in Figure 2b, maintains a linear

response in the entire range of the applied magnetic field (up to 9 T). This observation conveys that the mobility of electrons and holes is not high in $MoTe_2$, as in e.g., NbP. [48] It is not uncommon to see such a quasi-linear unsaturated behavior of *N* in semimetals. [48] In fact, this behavior is also observed in WTe_2, a material at the other end of the $Mo_{1-x}W_xTe_2$ alloy spectrum. [50]

3.3. Thermoelectric properties at different W content

In order to investigate the effect of W addition, $Mo_{1-x}W_xTe_2$ alloys with $x = 0$, 0.02, 0.03, 0.08 that are in the pure 1T′ phase at room temperature [40] and then transition to the T_d phase at lower temperatures were studied. The addition of W results in a consistent drop in the resistivity of all the samples which is consistent with previous measurements. [42,56,57] The temperature dependence of the resistivity of these samples is shown in Figure 1b and Figure 3(a-c). As the sample temperature is increased from 50 K, an increasing trend ($\frac{d\rho(T)}{dT} > 0$) is observed in the resistivity. At room temperature, the resistivity of $1T' - MoTe_2$ is $32\ \mu\Omega \cdot m$ compared to $(7.5 - 10)\ \mu\Omega \cdot m$ [14,42,57] and $95\ \mu\Omega \cdot m$ [58] which were reported previously for similar samples. Between 200 K to 300 K, all the samples show hysteresis as a consequence of the T_d to 1T′ phase transition. The center of the hysteresis loop shifts to higher temperatures with an increased molar fraction of W which is consistent with an earlier study. [42] Using $d\rho(T)/dT$ maxima for the cooling half-cycle, $1T'-T_d$ transition temperatures T_s of 240 K, 241 K, 250 K and 258 K are estimated for $MoTe_2$, $Mo_{0.98}W_{0.02}Te_2$, $Mo_{0.97}W_{0.03}Te_2$ and $Mo_{0.92}W_{0.08}Te_2$, respectively (see Figure S2 in the Supplemental Material). The shift in T_s occurs due to the interlayer contraction or expansion having the ability to enhance or weaken the hybridization of the Te p_z orbital. [57] Since the atomic size of W is slightly larger than the size of Mo, the addition of W increases the interlayer distance and weakens the hybridization. This results in an increase in the kinetic energy of the electrons and

consequently total energy of the 1T′ system. [59] As a result, the energy gap between the T_d and 1T′ phase increases causing a shift of the phase change to a higher temperature.

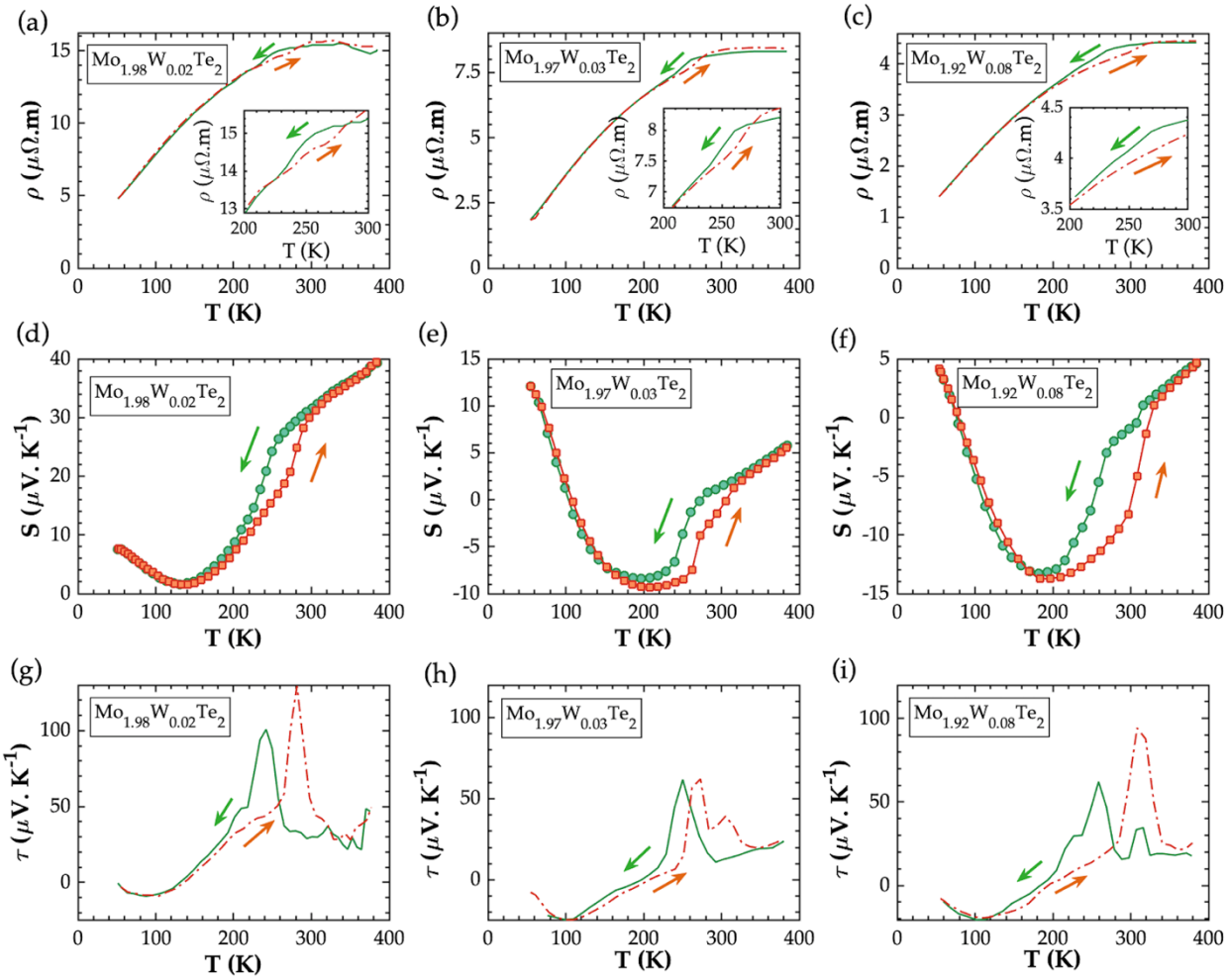

Figure 3 Temperature dependence of (a-c) resistivity, (d-f) Seebeck coefficient and (g-i) Thomson coefficient of $Mo_{0.98}W_{0.02}Te_2$, $Mo_{0.97}W_{0.03}Te_2$ and $Mo_{0.92}W_{0.08}Te_2$ over the cooling (solid line) and warming (dashed line) half-cycles

The temperature dependence of the Seebeck coefficient of all four samples from 55 K to 380 K is shown in Figure 1c and Figure 3(d-f). For all the samples, *S* is positive at 380 K and follows a resembling trend over the entire temperature range investigated. The magnitude of *S* for all these samples is small due to the semimetallic nature of the samples and the bipolar transport. For $MoTe_2$ and $Mo_{0.98}W_{0.02}Te_2$, *S* is positive throughout the entire temperature range. For the remaining two samples, we observe *S* to flip sign at an

intermediate temperature (110 K – 305 K for $Mo_{0.97}W_{0.03}Te_2$ and 78 K – 320 K for $Mo_{0.92}W_{0.08}Te_2$). The density functional theory (DFT) study has revealed that $MoTe_2$ has three interconnected hole pockets and four disconnected electron pockets with the electronic band structure remaining temperature independent from 20 K to 130 K. [7,8] The net size of the hole pockets has been reported to be larger than the net size of the electron pockets. [8] Additionally, with increasing temperature, the size of the electron pockets remains fairly constant while the hole pockets experience the largest change. Taking all these into account, qualitatively we can comment that our experimental results are in agreement with the DFT results as the *S* of the four samples exhibited predominantly positive behavior over the measured temperature range. The Fermi level changes with temperature, modifying the overall number of electrons and holes contributing to the transport. The valley observed in the Seebeck coefficient at the intermediate temperature is indicative of the competing nature of the electron hole-pockets as the temperature is changing. Like temperature, W addition can also result in moving the Fermi level. From Figure 3(d-f), we can see that the addition of W has gradually lowered the Seebeck coefficient minima recorded in the intermediate temperature range for $Mo_{0.98}W_{0.02}Te_2$, $Mo_{0.97}W_{0.03}Te_2$ and $Mo_{0.92}W_{0.08}Te_2$. Hence, the addition of W increases the contribution of the electron pockets possibly by lowering the size of the hole pockets, consequently lowering the overall Seebeck coefficient. The change in the relative electron-hole pockets can also be attributed to the Lifshitz transition as argued in Ref. 7. Accordingly, a topological reconstruction of the Fermi surface induces an anomaly in the Seebeck coefficient resulting in a change in the slope of the Seebeck coefficient with respect to temperature, dS/dT. Thomson coefficient as shown in Figure 3(g-i) remained higher than the Seebeck coefficient even after the addition of W. $Mo_{0.98}W_{0.02}Te_2$ exhibited the highest Thomson coefficient among these three alloys. Similar to the the phase transition temperature shifting to higher temperature in response

to an increased W addition, a gradual shift in the peak of Thomson coefficient is also observed.

4. Conclusion

We demonstrated that the Seebeck coefficient measurement is a better alternative than the resistivity measurement in probing the temperature-dependent $1T'-T_d$ phase transition in $MoTe_2$. This is because the carrier lifetime plays a major role in resistivity compared to the Seebeck coefficient. Centering around the temperature where the phase transition occurs, a high Thomson coefficient is observed. The absolute value of the Thomson coefficient in $MoTe_2$ is significantly larger than that of the Seebeck coefficient. The Nernst coefficient in $MoTe_2$, has a topologically induced peak value of 0.82 $\mu VK^{-1}T^{-1}$ at approximately 25 K that occurs as a consequence of the position of the Fermi level coinciding with the position of the Dirac points. Investigating the effect of W substitution on the thermoelectric properties of $Mo_{1-x}W_xTe_2$, we observed that an increased W content, from x = 0.02 to x = 0.08, made the samples more electron-dominant as is evident in the Seebeck measurements, and consistently lowered the resistivity of both $1T'$ and T_d phases. Seebeck coefficient measurement revealed the competing nature of the electron and hole pockets as we change the temperature or alloy $MoTe_2$ with W.

Data availability

The data that support the findings of this study are available from the corresponding author upon reasonable request.

Credit author statement

Md Sabbir Akhanda: Investigation, Data curation, Validation, Formal analysis, Visualization, Writing-original draft. **Sergiy Krylyuk:** Resources, Writing - Review &

Editing. **Diane A. Dickie:** Investigation. **Albert V. Davydov:** Resources, Writing - Review & Editing, Funding acquisition. **Fei Han:** Investigation. **Mingda Li:** Resources. **Mona Zebarjadi:** Conceptualization, Validation, Formal analysis, Resources, Writing - Review & Editing, Supervision, Funding acquisition.

Declaration of competing interest

The authors declare that they have no known competing financial interests or personal relationships that could have appeared to influence the work reported in this article.

Acknowledgments

This work is supported in part by DOE-SBIR contract # DE-SC0019552. S.K. and A.V.D. acknowledge support from Material Genome Initiative funding allocated to NIST.

Disclaimer

Certain commercial equipment, instruments, or materials are identified in this paper in order to specify the experimental procedure adequately. Such identification is not intended to imply recommendation or endorsement by the National Institute of Standards and Technology, nor is it intended to imply that the materials or equipment identified are necessarily the best available for the purpose.

References

[1] A. A. Al-Hilli and B. L. Evans, *The Preparation and Properties of Transition Metal Dichalcogenide Single Crystals*, J. Cryst. Growth **15**, 93 (1972).

[2] W. G. Dawson and D. W. Bullett, *Electronic Structure and Crystallography of MoTe 2 and WTe 2*, J. Phys. C Solid State Phys. **20**, 6159 (1987).

[3] X. Zhang, S. Y. Teng, A. C. M. Loy, B. S. How, W. D. Leong, and X. Tao, *Transition Metal Dichalcogenides for the Application of Pollution Reduction: A Review*,

Nanomaterials **10**, 1012 (2020).
[4] H. Weyl, *Gravitation and the Electron*, Proc. Natl. Acad. Sci. **15**, 323 (1929).
[5] A. A. Burkov, *Topological Semimetals*, Nat. Mater. **15**, 1145 (2016).
[6] S.-Y. Xu, I. Belopolski, N. Alidoust, M. Neupane, G. Bian, C. Zhang, R. Sankar, G. Chang, Z. Yuan, C.-C. Lee, S.-M. Huang, H. Zheng, J. Ma, D. S. Sanchez, B. Wang, A. Bansil, F. Chou, P. P. Shibayev, H. Lin, S. Jia, and M. Z. Hasan, *Discovery of a Weyl Fermion Semimetal and Topological Fermi Arcs.*, Science **349**, 613 (2015).
[7] F. C. Chen, H. Y. Lv, X. Luo, W. J. Lu, Q. L. Pei, G. T. Lin, Y. Y. Han, X. B. Zhu, W. H. Song, and Y. P. Sun, *Extremely Large Magnetoresistance in the Type-II Weyl Semimetal $MoTe_2$*, Phys. Rev. B **94**, 235154 (2016).
[8] S. Thirupathaiah, R. Jha, B. Pal, J. S. Matias, P. K. Das, P. K. Sivakumar, I. Vobornik, N. C. Plumb, M. Shi, R. A. Ribeiro, and D. D. Sarma, *$MoTe_2$: An Uncompensated Semimetal with Extremely Large Magnetoresistance*, Phys. Rev. B **95**, 241105 (2017).
[9] J. Yang, J. Colen, J. Liu, M. C. Nguyen, G. Chern, and D. Louca, *Elastic and Electronic Tuning of Magnetoresistance in MoTe 2*, Sci. Adv. **3**, eaao4949 (2017).
[10] M. N. Ali, J. Xiong, S. Flynn, J. Tao, Q. D. Gibson, L. M. Schoop, T. Liang, N. Haldolaarachchige, M. Hirschberger, N. P. Ong, and R. J. Cava, *Large, Non-Saturating Magnetoresistance in WTe_2*, Nature **514**, 205 (2014).
[11] Y. Wang, E. Liu, H. Liu, Y. Pan, L. Zhang, J. Zeng, Y. Fu, M. Wang, K. Xu, Z. Huang, Z. Wang, H. Z. Lu, D. Xing, B. Wang, X. Wan, and F. Miao, *Gate-Tunable Negative Longitudinal Magnetoresistance in the Predicted Type-II Weyl Semimetal WTe_2*, Nat. Commun. **7**, 1 (2016).
[12] E. Zhang, R. Chen, C. Huang, J. Yu, K. Zhang, W. Wang, S. Liu, J. Ling, X. Wan, H. Z. Lu, and F. Xiu, *Tunable Positive to Negative Magnetoresistance in Atomically Thin WTe_2*, Nano Lett. **17**, 878 (2017).
[13] J. X. Gong, J. Yang, M. Ge, Y. J. Wang, D. D. Liang, L. Luo, X. Yan, W. L. Zhen, S. R. Weng, L. Pi, C. J. Zhang, and W. K. Zhu, *Non-Stoichiometry Effects on the Extreme Magnetoresistance in Weyl Semimetal WTe_2*, Chinese Phys. Lett. **35**, 097101 (2018).
[14] Y. Qi, P. G. Naumov, M. N. Ali, C. R. Rajamathi, W. Schnelle, O. Barkalov, M. Hanfland, S. C. Wu, C. Shekhar, Y. Sun, V. Süß, M. Schmidt, U. Schwarz, E. Pippel, P. Werner, R. Hillebrand, T. Förster, E. Kampert, S. Parkin, R. J. Cava, C. Felser, B. Yan, and S. A. Medvedev, *Superconductivity in Weyl Semimetal Candidate $MoTe_2$*, Nat. Commun. **7**, 1 (2016).
[15] C. Heikes, I. L. Liu, T. Metz, C. Eckberg, P. Neves, Y. Wu, L. Hung, P. Piccoli, H. Cao, J. Leao, J. Paglione, T. Yildirim, N. P. Butch, and W. Ratcliff, *Mechanical Control of Crystal Symmetry and Superconductivity in Weyl Semimetal $MoTe_2$*, Phys. Rev. Mater. **2**, 74202 (2018).
[16] W. Wang, S. Kim, M. Liu, F. A. Cevallos, R. J. Cava, and N. P. Ong, *Evidence for an Edge Supercurrent in the Weyl Superconductor $MoTe_2$*, Science **368**, 534 (2020).

[17] P. Lu, J. S. Kim, J. Yang, H. Gao, J. Wu, D. Shao, B. Li, D. Zhou, J. Sun, D. Akinwande, D. Xing, and J. F. Lin, *Origin of Superconductivity in the Weyl Semimetal WTe_2 under Pressure*, Phys. Rev. B **94**, 224512 (2016).

[18] Y. T. Chan, P. L. Alireza, K. Y. Yip, Q. Niu, K. T. Lai, and S. K. Goh, *Nearly Isotropic Superconductivity in the Layered Weyl Semimetal WTe_2 at 98.5 Kbar*, Phys. Rev. B **96**, 180504 (2017).

[19] C. Huang, A. Narayan, E. Zhang, Y. Liu, X. Yan, J. Wang, C. Zhang, W. Wang, T. Zhou, C. Yi, S. Liu, J. Ling, H. Zhang, R. Liu, R. Sankar, F. Chou, Y. Wang, Y. Shi, K. T. Law, S. Sanvito, P. Zhou, Z. Han, and F. Xiu, *Inducing Strong Superconductivity in WTe_2 by a Proximity Effect*, ACS Nano **12**, 7185 (2018).

[20] Q. Li, C. He, Y. Wang, E. Liu, M. Wang, Y. Wang, J. Zeng, Z. Ma, T. Cao, C. Yi, N. Wang, K. Watanabe, T. Taniguchi, L. Shao, Y. Shi, X. Chen, S. J. Liang, Q. H. Wang, and F. Miao, *Proximity-Induced Superconductivity with Subgap Anomaly in Type II Weyl Semi-Metal WTe_2*, Nano Lett. **18**, 7962 (2018).

[21] D. D. Liang, Y. J. Wang, W. L. Zhen, J. Yang, S. R. Weng, X. Yan, Y. Y. Han, W. Tong, W. K. Zhu, L. Pi, and C. J. Zhang, *Origin of Planar Hall Effect in Type-II Weyl Semimetal $MoTe_2$*, AIP Adv. **9**, 055015 (2019).

[22] P. Li, C. Zhang, Y. Wen, L. Cheng, G. Nichols, D. G. Cory, G. X. Miao, and X. X. Zhang, *Anisotropic Planar Hall Effect in the Type-II Topological Weyl Semimetal WTe_2*, Phys. Rev. B **100**, 205128 (2019).

[23] B. Zhao, D. Khokhriakov, Y. Zhang, H. Fu, B. Karpiak, A. M. Hoque, X. Xu, Y. Jiang, B. Yan, and S. P. Dash, *Observation of Charge to Spin Conversion in Weyl Semimetal WTe_2 at Room Temperature*, Phys. Rev. Res. **2**, 13286 (2020).

[24] R. A. John, J. Acharya, C. Zhu, A. Surendran, S. K. Bose, A. Chaturvedi, N. Tiwari, Y. Gao, Y. He, K. K. Zhang, M. Xu, W. L. Leong, Z. Liu, A. Basu, and N. Mathews, *Optogenetics Inspired Transition Metal Dichalcogenide Neuristors for In-Memory Deep Recurrent Neural Networks*, Nat. Commun. **11**, 3211 (2020).

[25] X. J. Yan, Y. Y. Lv, L. Li, X. Li, S. H. Yao, Y. Bin Chen, X. P. Liu, H. Lu, M. H. Lu, and Y. F. Chen, *Composition Dependent Phase Transition and Its Induced Hysteretic Effect in the Thermal Conductivity of $W_xMo_{1-x}Te_2$*, Appl. Phys. Lett. **110**, (2017).

[26] A. Crepaldi, G. Autès, A. Sterzi, G. Manzoni, M. Zacchigna, F. Cilento, I. Vobornik, J. Fujii, P. Bugnon, A. Magrez, H. Berger, F. Parmigiani, O. V. Yazyev, and M. Grioni, *Persistence of a Surface State Arc in the Topologically Trivial Phase of $MoTe_2$*, Phys. Rev. B **95**, 041408 (2017).

[27] J. Jiang, Z. K. Liu, Y. Sun, H. F. Yang, C. R. Rajamathi, Y. P. Qi, L. X. Yang, C. Chen, H. Peng, C. C. Hwang, S. Z. Sun, S. K. Mo, I. Vobornik, J. Fujii, S. S. P. Parkin, C. Felser, B. H. Yan, and Y. L. Chen, *Signature of Type-II Weyl Semimetal Phase in $MoTe_2$*, Nat. Commun. **8**, 1 (2017).

[28] K. Deng, G. Wan, P. Deng, K. Zhang, S. Ding, E. Wang, M. Yan, H. Huang, H. H. Zhang, Z. Xu, J. Denlinger, A. Fedorov, H. Yang, W. Duan, H. Yao, Y. Wu, S. Fan,

H. H. Zhang, X. Chen, and S. Zhou, *Experimental Observation of Topological Fermi Arcs in Type-II Weyl Semimetal $MoTe_2$*, Nat. Phys. **12**, 1105 (2016).

[29] L. Huang, T. M. McCormick, M. Ochi, Z. Zhao, M. T. Suzuki, R. Arita, Y. Wu, D. Mou, H. Cao, J. Yan, N. Trivedi, and A. Kaminski, *Spectroscopic Evidence for a Type II Weyl Semimetallic State in $MoTe_2$*, Nat. Mater. **15**, 1155 (2016).

[30] I. Belopolski, S. Y. Xu, Y. Ishida, X. Pan, P. Yu, D. S. Sanchez, H. Zheng, M. Neupane, N. Alidoust, G. Chang, T. R. Chang, Y. Wu, G. Bian, S. M. Huang, C. C. Lee, D. Mou, L. Huang, Y. Song, B. Wang, G. Wang, Y. W. Yeh, N. Yao, J. E. Rault, P. Le Fèvre, F. Bertran, H. T. Jeng, T. Kondo, A. Kaminski, H. Lin, Z. Liu, F. Song, S. Shin, and M. Z. Hasan, *Fermi Arc Electronic Structure and Chern Numbers in the Type-II Weyl Semimetal Candidate $Mo_xW_{1-x}Te_2$*, Phys. Rev. B **94**, 085127 (2016).

[31] I. Belopolski, D. S. Sanchez, Y. Ishida, X. Pan, P. Yu, S. Y. Xu, G. Chang, T. R. Chang, H. Zheng, N. Alidoust, G. Bian, M. Neupane, S. M. Huang, C. C. Lee, Y. Song, H. Bu, G. Wang, S. Li, G. Eda, H. T. Jeng, T. Kondo, H. Lin, Z. Liu, F. Song, S. Shin, and M. Zahid Hasan, *Discovery of a New Type of Topological Weyl Fermion Semimetal State in $Mo_xW_{1-x}Te_2$*, Nat. Commun. **7**, 1 (2016).

[32] S. Jia, S.-Y. Xu, and M. Z. Hasan, *Weyl Semimetals, Fermi Arcs and Chiral Anomalies*, Nat. Mater. **15**, 1140 (2016).

[33] H. Zheng and M. Z. Hasan, *Quasiparticle Interference on Type-I and Type-II Weyl Semimetal Surfaces: A Review*, Advances in Physics: X.

[34] D. Puotinen and R. E. Newnham, *The Crystal Structure of $MoTe_2$*, Acta Crystallogr. **14**, 691 (1961).

[35] B. E. Brown, *The Crystal Structures of WTe_2 and High-Temperature $MoTe_2$*, Acta Crystallogr. **20**, 268 (1966).

[36] R. Clarke, E. Marseglia, and H. P. Hughes, *A Low-Temperature Structural Phase Transition in β-$MoTe_2$*, Philos. Mag. B Phys. Condens. Matter; Stat. Mech. Electron. Opt. Magn. Prop. **38**, 121 (1978).

[37] J. C. Park, S. J. Yun, H. Kim, J. H. Park, S. H. Chae, S. J. An, J. G. Kim, S. M. Kim, K. K. Kim, and Y. H. Lee, *Phase-Engineered Synthesis of Centimeter-Scale 1T′- and 2H-Molybdenum Ditelluride Thin Films*, ACS Nano **9**, 6548 (2015).

[38] T.-R. Chang, S.-Y. Xu, G. Chang, C.-C. Lee, S.-M. Huang, B. Wang, G. Bian, H. Zheng, D. S. Sanchez, I. Belopolski, N. Alidoust, M. Neupane, A. Bansil, H.-T. Jeng, H. Lin, and M. Zahid Hasan, *Prediction of an Arc-Tunable Weyl Fermion Metallic State in $Mo_xW_{1-x}Te_2$*, Nat. Commun. **7**, 10639 (2016).

[39] A. N. Domozhirova, A. A. Makhnev, E. I. Shreder, S. V. Naumov, A. V. Lukoyanov, V. V. Chistyakov, J. C. A. Huang, A. A. Semiannikova, P. S. Korenistov, and V. V. Marchenkov, *Electronic Properties of WTe_2 and $MoTe_2$ Single Crystals*, J. Phys. Conf. Ser. **1389**, 012149 (2019).

[40] S. M. Oliver, R. Beams, S. Krylyuk, I. Kalish, A. K. Singh, A. Bruma, F. Tavazza, J. Joshi, I. R. Stone, S. J. Stranick, A. V. Davydov, and P. M. Vora, *The Structural*

Phases and Vibrational Properties of $Mo_{1-x}W_xTe_2$ Alloys, 2D Mater. **4**, (2017).
[41] H. J. Kim, S. H. Kang, I. Hamada, and Y. W. Son, *Origins of the Structural Phase Transitions in MoTe2 and WTe2*, Phys. Rev. B **95**, 180101 (2017).
[42] R. Dahal, L. Z. Deng, N. Poudel, M. Gooch, Z. Wu, H. C. Wu, H. D. Yang, C. K. Chang, and C. W. Chu, *Tunable Structural Phase Transition and Superconductivity in the Weyl Semimetal $Mo_{1-x}W_xTe_2$*, Phys. Rev. B **101**, 140505 (2020).
[43] R. Modak, M. Murata, D. Hou, A. Miura, R. Iguchi, B. Xu, R. Guo, J. Shiomi, Y. Sakuraba, and K. I. Uchida, *Phase-Transition-Induced Giant Thomson Effect for Thermoelectric Cooling*, Appl. Phys. Rev. **9**, 011414 (2022).
[44] W. Thomson, *4. On a Mechanical Theory of Thermo-Electric Currents.*, Proc. R. Soc. Edinburgh **3**, 91 (1857).
[45] K. I. Uchida, M. Murata, A. Miura, and R. Iguchi, *Observation of the Magneto-Thomson Effect*, Phys. Rev. Lett. **125**, 106601 (2020).
[46] H. Reith, K. Nielsch, N. F. Hinsche, F. Rittweger, M. Hölzer, P. Zahn, A. Ernst, and I. Mertig, *Ab Initio Description of the Thermoelectric Properties of Heterostructures in the Diffusive Limit of Transport*, Physica Status Solidi (A) Applications and Materials Science.
[47] A. v. Ettingshausen and W. Nernst, *Ueber Das Auftreten Electromotorischer Kräfte in Metallplatten, Welche von Einem Wärmestrome Durchflossen Werden Und Sich Im Magnetischen Felde Befinden*, Ann. Der Phys. Und Chemie **265**, 343 (1886).
[48] S. J. Watzman, T. M. Mccormick, C. Shekhar, S.-C. C. Wu, Y. Sun, A. Prakash, C. Felser, N. Trivedi, and J. P. Heremans, *Dirac Dispersion Generates Unusually Large Nernst Effect in Weyl Semimetals*, Phys. Rev. B **97**, 161404 (2018).
[49] J. Sen Xiang, S. Le Hu, M. Lyu, W. L. Zhu, C. Y. Ma, Z. Y. Chen, F. Steglich, G. F. Chen, and P. J. Sun, *Large Transverse Thermoelectric Figure of Merit in a Topological Dirac Semimetal*, Sci. China Physics, Mech. Astron. **63**, 237011 (2020).
[50] K. G. Rana, F. K. Dejene, N. Kumar, C. R. Rajamathi, K. Sklarek, C. Felser, and S. S. P. Parkin, *Thermopower and Unconventional Nernst Effect in the Predicted Type-II Weyl Semimetal WTe_2*, Nano Lett. **18**, 6591 (2018).
[51] F. Han, N. Andrejevic, T. Nguyen, V. Kozii, Q. T. Nguyen, T. Hogan, Z. Ding, R. Pablo-Pedro, S. Parjan, B. Skinner, A. Alatas, E. Alp, S. Chi, J. Fernandez-Baca, S. Huang, L. Fu, and M. Li, *Quantized Thermoelectric Hall Effect Induces Giant Power Factor in a Topological Semimetal*, Nat. Commun. **11**, 1 (2020).
[52] M. S. Akhanda, S. E. Rezaei, K. Esfarjani, S. Krylyuk, A. V. Davydov, and M. Zebarjadi, *Thermomagnetic Properties of Bi2Te3 Single Crystal in the Temperature Range from 55 K to 380 K THERMOMAGNETIC PROPERTIES of Bi2Te3 ... MD SABBIR AKHANDA et Al.*, Phys. Rev. Mater. **5**, 015403 (2021).
[53] M. Zebarjadi, S. E. Rezaei, M. S. Akhanda, and K. Esfarjani, *Nernst Coefficient within Relaxation Time Approximation*, Phys. Rev. B **103**, 144404 (2021).
[54] K. Behnia, M.-A. Méasson, and Y. Kopelevich, *Nernst Effect in Semimetals: The*

Effective Mass and the Figure of Merit, Phys. Rev. Lett. **98**, 076603 (2007).

[55] H. Jones and C. Zener, *The Theory of the Change in Resistance in a Magnetic Field*, Proc. R. Soc. London. Ser. A, Contain. Pap. a Math. Phys. Character **145**, 268 (1934).

[56] H. Sakai, K. Ikeura, M. S. Bahramy, N. Ogawa, D. Hashizume, J. Fujioka, Y. Tokura, and S. Ishiwata, *Critical Enhancement of Thermopower in a Chemically Tuned Polar Semimetal $MoTe_2$*, Sci. Adv. **2**, e1601378 (2016).

[57] K. Ikeura, H. Sakai, M. S. Bahramy, and S. Ishiwata, *Rich Structural Phase Diagram and Thermoelectric Properties of Layered Tellurides $Mo_{1-x}Nb_xTe_2$*, APL Mater. **3**, 41514 (2015).

[58] S. Paul, S. Karak, M. Mandal, A. Ram, S. Marik, R. P. Singh, and S. Saha, *Tailoring the Phase Transition and Electron-Phonon Coupling in 1T'-$MoTe_2$ by Charge Doping: A Raman Study*, Phys. Rev. B **102**, 054103 (2020).

[59] H. Takahashi, T. Akiba, K. Imura, T. Shiino, K. Deguchi, N. K. Sato, H. Sakai, M. S. Bahramy, and S. Ishiwata, *Anticorrelation between Polar Lattice Instability and Superconductivity in the Weyl Semimetal Candidate $MoTe_2$*, Phys. Rev. B **95**, 100501 (2017).